Rocking chair-like movement of ex-solved nanoparticles on the Ni-Co doped $La_{0.6}Ca_{0.4}FeO_{3-\delta}$ oxygen carrier during chemical looping reforming coupled with CO_2 splitting

DongHwan Oh [a,1], Filippo Colombo [b,1], Luca Nodari [c,d], Jun Hyuk Kim [e], Jun Kyu Kim [a], Siwon Lee [f], Seunghyun Kim [a], Sangwoo Kim [a], Dae-Kwang Lim [g], Jongsu Seo [h], Sejong Ahn [a], Simone Mascotto [b,*], WooChul Jung [a,*]

[a] Department of Materials Science and Engineering, Korea Advanced Institute of Science and Technology (KAIST), Daejeon 34141, Republic of Korea
[b] Institut für Anorganische und Angewandte Chemie, Universität Hamburg, Hamburg 20146, Germany
[c] Department of Chemical Science, University of Padua, Padova 35131, Italy
[d] Institute of Condensed Matter Chemistry and Technologies for Energy, National Research Council, Padova 35127, Italy
[e] Department of Chemical Engineering, Hongik University, Seoul 04066, Republic of Korea
[f] Department of Materials Science and Engineering, Hanbat National University, Daejeon 34158, Republic of Korea
[g] KEPCO Research Institute, Daejeon 34056, Republic of Korea
[h] Hydrogen Research Department, Korea Institute of Energy Research (KIER), Daejeon 34129, Republic of Korea

ARTICLE INFO

ABSTRACT

Chemical looping reforming coupled with CO_2 splitting is a promising CO_2 utilization method that produces a valuable fuel. Here, we present a novel perovskite oxide with the composition of $La_{0.6}Ca_{0.4}Fe_{0.95}M_{0.05}O_{3-\delta}$ (M = Ni, Co, Ni-Co) that functions both as an oxygen carrier and as a redox catalyst. Using a multi technique approach with HR-TEM, XRD, XAS, and Mössbauer spectroscopy, we find that alloy nanoparticles spontaneously form on the surface of Ni-Co doped carriers in a CH_4 atmosphere, and as they are repeatedly exposed to CO_2 and CH_4 during the chemical loop, Fe atoms move back and forth between the inside (as Fe cations in the lattice) and the outside (as a part of metallic alloy) of the host scaffold. Eventually, the co-doped samples become highly reactive towards both gases and have excellent coking and redox stability, demonstrating record-level syngas yield (total ~10 mmol/g) at 850 °C, over 50 redox cycles.

1. Introduction

The carbon footprint engraved by the tremendous use of carbon-positive energy sources leads to the rapid increase of CO_2 levels in the atmosphere. Hence, excessive researches are underway to alternate old-fashioned energy production with a sustainable route. Among the several approaches, CO_2 capture, utilization, and storage (CCUS) are considered a core strategy capable of reducing CO_2 while promoting sustainability in the present industry. In particular, the chemical looping process is one such representatives of it that can simultaneously capture CO_2 while producing desired products (e.g., energy, pure oxygen, syngas, ethylene) with high yield. It was also announced that chemical looping has been selected as a major project for advanced combustion systems by the U.S. department of energy (DOE). [1].

Meanwhile, the depletion of petroleum and the increasing access to natural gases (e.g., shale gas) are driving interest in converting natural gas to syngas. [2–4] Syngas is a mixture of CO and H_2 and is widely used in industrial chemistry as a building unit in the Fischer-Tropsch synthesis process. [5] Moreover, its storage flexibility and immediate applicability as a fuel deem syngas a useful energy resource. A representative example of its usefulness is that it can be directly injected as a fuel into solid oxide cells, a promising energy production technology, without additional reforming equipment. [6–8] Thus far, considerable research has been conducted to produce syngas from methane, which accounts for the largest share of natural gas. In particular, the partial oxidation of methane (POM) is advantageous for maintaining the ideal

product gas composition (i.e., an H_2-to-CO ratio of 2) when synthesizing hydrocarbons such as gasoline and methanol. However, because POM is based on a direct reaction between oxygen and fuel, it is explosive and produces noxious gases such as NO_x, thus requiring an additional purification process to supply oxygen. [9] To overcome these drawbacks, chemical looping reforming (CLR) is emerging as a promising alternative. CLR uses metal oxide carriers to provide oxygen and thus always separates methane and oxygen while retaining all of the advantages of oxy-combustion. CLR repeats a two-step isothermal process: (1) a fuel-supplying process in which lattice oxygen reacts with methane to produce synthesis gas, and (2) an oxygen-supplying process that involves the injection of oxidant gases into the reactor to fill oxygen vacancies in the carrier lattice. Here, when carbon dioxide is used as an oxidizing agent in step (2), it is possible not only additionally to generate CO but also to consume CO_2, thereby becoming a new route for CO_2 utilization. [10–12].

Indeed, the key to this strategy, combining CLR and CO_2 splitting, is to develop oxygen carriers with both decent reactivity, oxygen storage capacities, coking and redox durability. [13] Among reported carrier materials, perovskite oxides have attracted much interest, as their composition flexibility results in chemical and structural versatility. For example, the substitution of proper amounts of elements with a lower oxidation state (i.e., Sr^{2+}, Nd^{2+}) onto La^{3+} in lanthanum ferrite leads to enhanced CO selectivity, methane activation, and oxygen storage capacity. Further research has established that $La_{1-x}Sr_xFeO_{3-\delta}$ is a promising candidate for CLR. [14–17] However, strontium (Sr) is rare, expensive, and its segregation at high temperatures is known to cause permanent degradation in surface oxygen exchange kinetics. [18–21] To replace Sr, less expensive and earth-abundant calcium (Ca) substitution on $LaFeO_{3-\delta}$ has been assessed as a new redox catalyst route. Lim et al. proved the potential of $La_{0.6}Ca_{0.4}FeO_{3-\delta}$ as an oxygen carrier for chemical looping syngas generation. [22] Additionally, Ca^{2+} and La^{3+} have similar ionic radii and are more stable with respect to Sr substitution. [23] Despite the potential of Ca-substituted $LaFeO_3$, only a few reports have characterized its chemical looping properties thus far. Furthermore, no attempt has been made to improve the catalytic activity by reshaping the catalyst surface; therefore, the true value of $La_{0.6}Ca_{0.4}FeO_{3-\delta}$ remains behind the curtain.

In parallel with the above points, as an exclusive method by which to decorate oxide surfaces with well-dispersed metal nanoparticles, the 'ex-solution' process is now widely considered a novel process that can overcome the sluggish reaction hurdle associated with a heterogeneous catalyst. [24–26] Ex-solution is a process of spontaneously forming metal nanoparticles on the surface of a host oxide with only one reduction heat treatment, and is based on the selective phase separation of the surface of the composite oxide. It is currently gaining a great deal of recognition owing to the simplicity of the process and the excellent stability of the resulting particles. One of the ground-breaking features of ex-solution catalysts is their ability to regenerate spent catalyst into their initial state by conducting oxidizing annealing process. Here, the agglomerated surface nanoparticle goes back into the lattice as an ion state while it can be also move forth to the surface with additional reduction treatment. Since the CLR process involves repeatedly exposing the oxygen carrier to the high-temperature redox condition, in situ emergence of nanoparticles can occur in the reducing step, whereas the nanoparticle could go back through the host lattice in an oxidizing period. Recent studies have also suggested that a surface modification with ex-solved nanoparticles over a perovskite oxide could improve syngas production with superior stability during the CLR process. [27–29].

Motivated by these findings, we propose $La_{0.6}Ca_{0.4}FeO_{3-\delta}$, to which the concept of ex-solution is applied as a potent oxygen carrier for CLR-CO_2 splitting. Ni and Co (5 at%) are selected as a single or double dopant, and they are designed to precipitate themselves on the host surface during the CH_4 activation process. When Ni and Co are co-doped, the sample effectively shows lower activation temperatures for

CH_4 and CO_2 with an increased degree of carbon coking resistance. It is worth noting that the Fe-Ni-Co alloy (representative of various types of ex-solved nanoparticles) spontaneously formed on the host surface under the CH_4 atmosphere. The nanoparticles were switched into a Ni-Co alloy under CO_2 conditions by the voluntary reincorporation of Fe into the host lattice. The self-controlled nanoparticle composition in which Fe dynamically evolves iteratively recreates the appropriate catalyst for each redox reaction. As a result, the co-doped carrier shows a benchmark-level of syngas production both in CLR and CO_2 splitting. These observations revisit the potential of a Sr-free perovskite oxide for redox catalysts and suggest a novel strategy for designing ex-solved nanoparticles.

2. Experimental procedures

2.1. Catalyst preparation

$La_{0.6}Ca_{0.4}Fe_{0.95}M_{0.05}O_{3-\delta}$ (M = Ni, Co, Ni-Co) was synthesized by the sol-gel method with conventional nitrate precursors. $La(NO_3)_3 \cdot 6 H_2O$, $Ca(NO_3)_2 \cdot 4 H_2O$, $Ni(NO_3)_2 \cdot 6 H_2O$, $Co(NO_3)_2 \cdot 6 H_2O$ (Alfa Aesar), and Fe $(NO_3)_3 \cdot 9 H_2O$ (Sigma Aldrich) were completely dissolved in deionized water with citric acid (Junsei) as a chelating agent, at a stoichiometric ratio of metal ions:citric acid = 1:1.1. The solution was stirred at 25 °C for 30 min to form a homogeneous solution. The pH of the solution was adjusted to 7 using NH_4OH (Junsei) and kept at 230 °C until the solution turned into a dried gel. Then, the dried gel was heated for 3 h at 450 °C to burn any residual carbons. The calcination step was performed at 900 °C for 5 h with a ramping rate of 4 °C/min. The sample was pelletized in a uniaxial press, and immediately sintered at 1150 °C for 5 h.

2.2. Characterization of physical property

The crystal structure of the synthesized sample was analyzed through a high-resolution powder X-ray diffraction (HR-XRD, Rigaku SmartLab, Japan) with Cu-Kα radiation (λ = 1.5406 Å) at 45 kV, 200 mA, and a scan rate of 10°/min from 20° to 80°. The crystallite size was calculated with the most intense (002) peak using the Scherrer equation. Brunauer-Emmett-Teller specific surface area was measured through a Tristar II 3020 (Micromeritics, USA). The surface images of the prepared catalyst were observed using a Hitachi S-4800 (Japan) scanning electron microscope (SEM). Moreover, the composition of ex-solved nanoparticles was revealed via corrected scanning transmission electron microscopy (Cs-TEM) with a JEM-ARM200F (JEOL, Japan). Raman spectroscopy measurements were conducted by using an ARAMIS dispersive Raman spectrometer (Horiba Jobin Yvon, France). Raman spectra were recorded using 633 nm (HeNe) excitation laser lines. X-ray absorption spectra at the Fe K-edge (7.112 keV) were acquired at the Balder beamline of the Max IV Laboratory synchrotron in Lund, Sweden. A double crystal monochromator with Si(111) and Si(311) LN2-cooled crystals (doi:10.1088/1742–6596/712/1/012023) were employed for the energy scans around the respective metal absorption edge. The XAFS spectra were collected in transmission mode using gas ionization chambers to measure the photon intensities before and after the samples. The materials were diluted with cellulose, pressed into pellets and then covered in Kapton tape for the measurement via x-ray beam. The normalization of the obtained XAFS data was carried out by performing pre-edge and post-edge background subtraction in the Athena software using the AUBACK algorithm (Ravel, B.; Newville, M. IUCr. ATHENA, ARTEMIS, HEPHAESTUS: Data Analysis for X-Ray Absorption Spectroscopy Using IFEFFIT. J. Synchrotron Radiat. 2005, 12 (4), 537 – 541.) Room temperature Mössbauer spectroscopy was performed on a conventional constant acceleration spectrometer mounting a Rh matrix ^{57}Co source, nominal strength 1850 MBq. The hyperfine parameters were obtained by means of standard least-squares minimization techniques. The Mössbauer parameter δ is quoted relative to α-Fe foil.

2.3. Catalytic activity and redox property measurement

2.3.1. Calibration process for gas concentration

Prior to the real-time tracking with the quadrupole mass spectrometer (Pfeiffer vacuum, GSD 320) each reactant and product gases were calibrated with the targeted concentrations. All gases were diluted in Ar and $m/z = 40$ peak of Ar was chosen as a standard reference. The detailed gas concentration and monitored m/z peaks are as shown as follows. 5 vol% of CH_4 with $m/z = 16, 15, 14, 13,$ and 12 peaks. 5 vol% of CO_2 with $m/z = 44, 28, 16,$ and 12. 2 vol% of CO with $m/z = 29, 28,$ 16, and 12. 4 vol% of H_2 with $m/z = 2$.

2.3.2. Methane temperature-programmed reduction (MTPR)

To examine the reactivity of the prepared catalysts towards methane, MTPR was conducted in a quadrupole mass spectrometer equipped with a quartz type fixed-bed reactor (I.D. = 4 mm), packed with 100 mg of sample above the quartz wool. The K-type thermocouple was placed next to the quartz bed inside the vertical furnace. The ramp rate was 5 °C/min from 50 °C to 850 °C. 5 vol% of CH_4/Ar gas was used as the reactant gas at a flow rate of 50 sccm.

2.3.3. Methane pulse test

In order to evaluate the intrinsic properties of the $La_{0.6}Ca_{0.4}FeO_{3-\delta}$ based oxygen carrier, 200 mg of catalyst was loaded onto the quartz tube of the reactor to perform the transient-pulse study. 5% of CH_4/Ar (30 sccm) gas and Ar gas (30 sccm) was alternatively injected as a pulse 30 times under isothermal conditions (T_R = 850 °C). The CH_4 was pulsed for 1 min. To remove any residual gases from the previous CH_4 injection, Ar was pulsed for 3 min. The automated 4-way valve systems were used during the pulse test.

2.3.4. CO_2 temperature programmed oxidation (CO_2-TPO)

To measure the reactivity of the reduced samples towards CO_2, CO_2-TPO was performed after a hydrogen reduction treatment of the catalysts. Samples of 100 mg were loaded in the same reactor and annealed for 2 h at 700 °C under a 4% H_2/Ar atmosphere. Then, the reactor was cooled to 100 °C, and 5% of CO_2/Ar gas was continuously injected. After the stabilization of the CO_2 signal, the temperature was increased to 850 °C with a 10 °C/min ramping rate. The specific temperature was monitored, which corresponds to the CO evolution peak resulting from CO_2 splitting. Total flow rate was kept as 50 sccm.

2.3.5. CH_4 partial oxidation combined CO_2 splitting cycle

The redox experiment was repeated with 200 mg of the oxygen carriers. The reaction temperature reaches 850 °C under the CO_2 atmosphere (5% CO_2 in Ar). Then, the CH_4 reduction step (5% CH_4 in Ar) was maintained for 25 min to avoid coke formation. The CO_2 injection step was kept equally with the fuel oxidation period, and Ar purge was done for 3 min between each half redox cycle. Gas flow rate was maintained as 20 sccm and the automated 4-way valve systems were also adopted.

2.4. Data processing

By integrate the signal of gases with the time, amount of product gases was obtained using the below formulas.

$$N_{CO} = \int_{Red,Oxi} (y_{CO})_{outlet} ndt$$

$$N_{H_2} = \int_{Red} (y_{H_2})_{outlet} ndt$$

$$N_{CO_2} = \int_{Red,Oxi} (y_{CO_2})_{outlet} ndt$$

$$N_{CH_4} = \int_{Red} (y_{CH_4})_{outlet} ndt$$

Based on the above values, to compare the performance of each catalyst, CH_4 conversion (X_{CH_4}), oxygen storage capacity ($\Delta\delta$), CO Selectivity (S_{CO}), and CO_2 conversion (X_{CO_2}) were calculated with the following equations. The amount of produced water (N_{H_2O}) was estimated to be two times N_{CO_2} by considering the full oxidation of methane.

$$X_{CH_4} = \frac{N_{CH_4,inlet} - N_{CH_4,outlet}}{N_{CH_4,inlet}} \bullet 100$$

$$OSC(\Delta\delta) = \frac{(2N_{CO_2} + N_{CO} + N_{H_2O})}{mass\,of\,catalyst}$$

$$S_{CO} = \frac{N_{CO}}{N_{CO} + N_{CO_2}}$$

$$X_{CO_2} = \frac{N_{CO_2,inlet} - N_{CO_2,outlet}}{N_{CO_2,inlet}} \bullet 100$$

3. Results and discussion

3.1. Physical property of synthesized samples

Powder samples with the composition of $La_{0.6}Ca_{0.4}Fe_{0.95}M_{0.05}O_{3-\delta}$ (LCF 40) were synthesized as oxygen carriers through a sol-gel method. Fig. 1a shows the XRD patterns of the prepared samples with different compositions. Diffraction patterns reveal a single-phase orthorhombic crystal structure in all compositions without any second phase. Many studies have shown that the crystallite size and surface area of the oxygen carrier affect CO selectivity under a CH_4 atmosphere. [30] Thus, we used Scherrer's equation to calculate the crystallite sizes of our samples, with the BET surface areas also measured. As presented in Table S1, the differences in the crystallite sizes are negligible, and the surface area is maintained at less than 2 m²/g. These outcomes indicate there are no straightforward morphological changes related to the doping step, thus proving that our materials are the best testing ground for only considering surface chemistry changes. Fig. 1b displays the cleaved surface of the as-synthesized Ni-Co-doped sample. Given that no segregated particles or metal clusters were observed, the image also suggests that the dopants are well incorporated into the host oxide.

3.2. Interactions between the oxygen carriers and the reactant gases

A methane temperature-programmed reduction (MTPR) test was conducted to determine the CH_4 activation temperature and outlet gas composition. Fig. 2a shows the MTPR results of Ni-Co-doped LCF 40. Similar profiles were noted in all other samples. As the amount of produced CO_2 is negligible and considering that most of the CH_4 converted into CO (Fig. 2b-c), LCF 40 carriers are workable for the partial oxidation process as opposed to the combustion of methane. Doped carriers show noticeable syngas production even at approximately 700 °C, whereas the bare carrier only produces small amounts at temperatures above 800 °C, suggesting that doping is crucial for CH_4 activation. The Ni-doped sample exhibits the lowest CH_4 activation temperature, followed by the Ni-Co-doped, Co-doped, and bare samples (Fig. 2b). This observation is in good agreement with previous reports indicating that Ni has higher activity towards CH_4 than Co and that Fe is the least reactive. [31]

To achieve a specific insight into the CH_4 oxidation process, CH_4 gas was transiently injected at a short contact time to eliminate other complex reactions. [32] Monitoring the gas signal allows further investigations of the critical point of carbon coking, the CO selective regime, and degree of catalyst degradation. [33] Fig. 3a presents the result during the pulse reaction of the Ni-Co-doped oxygen carrier;
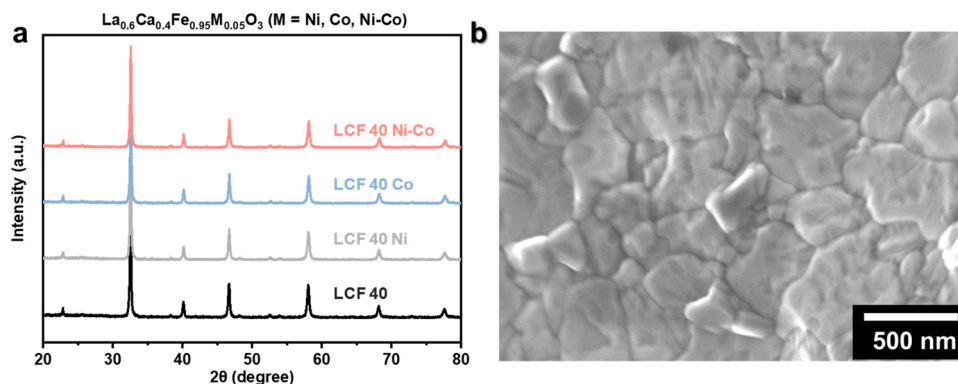
Fig. 1. Physical characterization of synthesized oxygen carrier (a) Powder X-ray diffraction patterns of synthesized oxygen carriers at varying dopant concentrations. (b) Cleaved surface images of as-synthesized Ni-Co-doped sample.
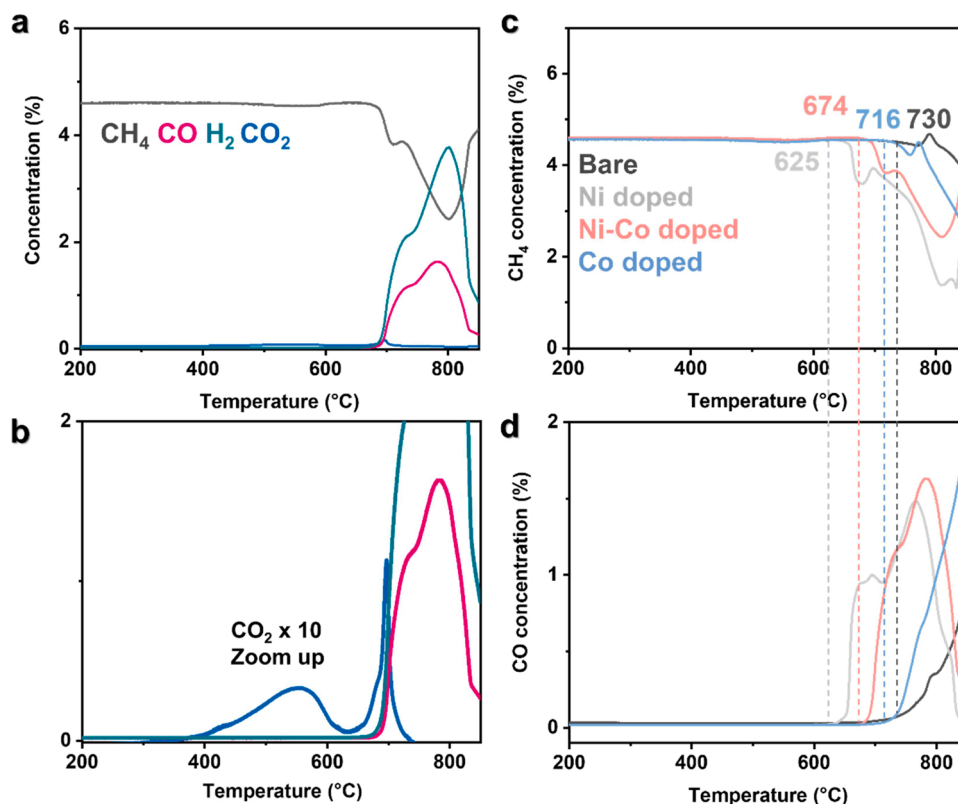

Fig. 2. Methane temperature programmed reduction result over $La_{0.6}Ca_{0.4}FeO_{3-\delta}$ based perovskite oxide under 5% CH_4/Ar condition (a) Overall product profile from Ni-Co doped sample versus temperature during the test. (b) Produced CO_2 stream with 10 times enlarged scale. (b) CH_4 concentration traces over the various type of samples. The inset number reveals the corresponding CH_4 activation temperature. (c) Outlet CO profile of each oxygen carrier.

similar trends were observed in the other carriers as well. In the early stages of the pulse test, CO_2 was the main product, which gradually decreased. Generally, oxygen on the surface (or weakly bound oxygen) mainly participates in the complete oxidation of CH_4. [34] Similarly, oxygen on the catalyst surface can drive the combustion until it is depleted. When the CO_2 signal begins to diminish, the CO signal continues to increase as a result of the partial oxidation of CH_4 with the lattice oxygen. The reactivity to CH_4 was measured in detail (Fig. 3b). Doping dramatically improves CH_4 conversion, and the Ni-doped sample showed the highest CH_4 conversion rate, even after the complete oxidation stage. In contrast, the Co-doped carrier shows low CH_4 conversion at the initial injection steps, which requires further pulses to activate and reaches the same conversion level as the Ni-doped one. The Ni-Co-doped sample is located between the Ni- and Co-doped cases,

which also coincide with our MTPR results. Fig. 3c shows the CO signals produced during the pulse tests of various oxygen carriers. The CO signal in the doped carriers begins to deteriorate (as indicated by the green arrow in Fig. 3c), which correlates with the occurrence of carbon coking. Here, considering the amounts of oxygen-containing products, oxygen storage capacity (OSC) can be obtained (Fig. 3d). Despite the fact that the Ni-doped sample shows the highest reactivity to CH_4, its low OSC make itself an unsuitable dopant. Its low OSC may be due to the lack of available oxygen, which cannot compete with the high activity of Ni towards CH_4. Moreover, by tracking the trends of H_2/CO ratio changes along the pulse number, we could further compare the coking resistance of the doped oxygen carrier (Fig. S1). While the Ni-Co doped and Co doped one shows similar trends with the CO peak evolution, Ni doped one shows rapid increase in H_2/CO ratio even at the seventh pulse
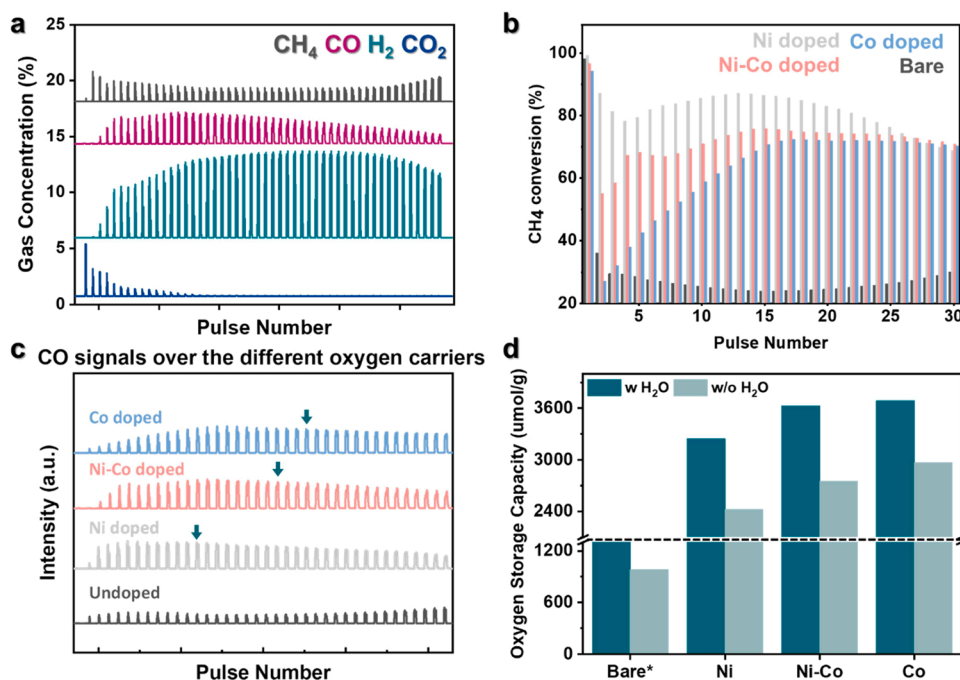
Fig. 3. Methane transient pulse test on the oxygen carriers (a) Outlet gas species during the pulse reaction from the Ni-Co-doped carrier. (b) CH_4 conversion of prepared samples over 30 pulses. (c) CO gas signals of the various oxygen carriers. The green arrow presents the specific moment where the CO signal decreases. (d) Oxygen storage capacity of doped oxygen carriers before the carbon coking occurs. (*Oxygen storage capacity of bare sample was calculated with the same pulse number with Ni-Co doped one.).

injection, which could be induced by the thermal cracking of CH_4. This might suggest that Ni doped one suffers from severe coke formation more than our expectation from the previous results. Thus, doping equimolar amounts of both Ni and Co (2.5 at% each) can significantly improve the CH_4 conversion rate as much as Ni doping and can make OSC comparable to that of the Co-doped sample.

After the screening process of oxygen carriers by evaluating the reactivity towards CH_4, the Ni-Co-doped sample was found to be an excellent candidate for reforming step. Then, we further demonstrate the reactivity of hydrogen-annealed oxygen carriers (bare and Ni-Co-doped carriers) with CO_2 via CO_2-TPO experiments. Fig. 4a shows the CO gas signal generated from CO_2 splitting versus the temperature. Initially ($\approx$100 °C), the CO gas signal was negligible in both the bare and Ni-Co-doped samples. However, the highest CO signal of the LCF 40 Ni-

Co carrier was observed at 533 °C, which is approximately 50 °C lower than that of the bare carrier. This suggests that only 5 at% co-doping can significantly improve the CO_2 splitting ability of the oxygen carrier. The evolution of the crystalline phase of the CO_2 treated samples was investigated using Raman spectra analysis. Both carrier samples showed spectra corresponding to a perovskite oxide lattice near 250–700 cm^{-1} in area. In contrast, while the co-doped carrier displayed only black powders, unknown brown particles were routinely observed in the pristine carrier (Fig. 4b-c). These particles were characterized as a Fe_3O_4 phase (Fig. 4e, $\nu = 288$, 620 cm^{-1}) and were not found in the co-doped carrier. To the best of our knowledge, iron oxide has rarely been adopted as a standalone oxygen carrier for CH_4 conversion owing to its low catalytic activity towards CH_4. [35] Therefore, we conclude that the bare sample is prone to separate into two phases under CO_2, with a
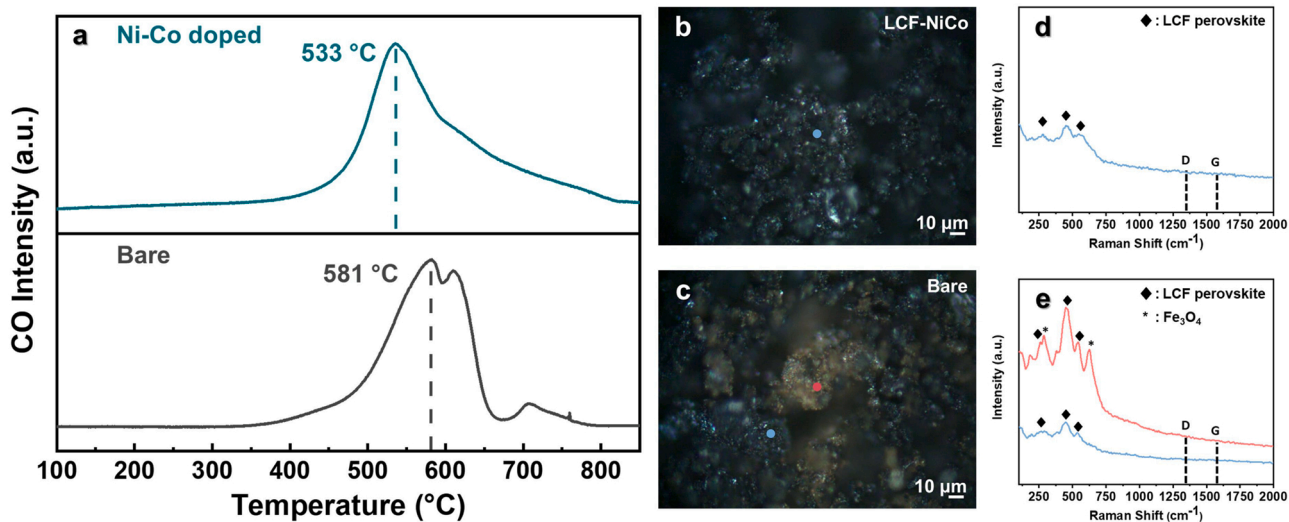

Fig. 4. Re-oxidation test of reduced oxygen carrier with 5 vol% CO_2 at a temperature range of 100–850 °C. (a) Profile of the CO stream generated from the CO_2-temperature programmed oxidation (CO_2-TPO) for pre-reduced (reduction condition: 4 vol% H_2, 700 °C, 2 h) oxygen carriers. Sample photographs (b) bare and (c) Ni-Co-doped. *Ex-situ* Raman spectra result after CO_2-TPO for (d) bare and (e) Ni-Co-doped catalyst. In plot (e), each colored graph corresponds to the specific points in (c), which indicates the scanned area for Raman spectra.

subsequent insufficient phase recovery. Moreover, because Fe is a primary component of the host perovskite oxide, its composition should be fully regenerated without bulk phase separation under the operating conditions to maintain its initial OSC. If not, the catalyst will permanently degrade as the redox cycles are repeated. [36,37] Eventually, doping enables CO_2 capturing and improves phase recoverability of oxygen carriers during the CO_2 splitting process, suggesting that doping will play a pivotal role in practical CLR-CO_2 splitting operations.

3.3. Multiple cycle test of selected oxygen carrier

As we have shown in the prior experiments, the Ni-Co-doped oxygen carrier exhibited excellent redox performance either in a CH_4 or a CO_2 atmosphere. To evaluate the multiple cycle properties with regard to chemical looping syngas production, the partial oxidation of CH_4 coupled with the CO_2 splitting redox cycle was performed at 850 °C (Fig. 5a-b and Fig. S2). On average, the gas conversion of Ni-Co-doped one reaches 70% with 90% CO selectivity while the pristine carrier shows 10% of gas conversion. Strikingly, its product yield in the 50th cycle was still greater than the product amount from the 1st cycle with the bare carrier. This implies a significant improvement in both the durability and reactivity of the Ni-Co-doped catalyst. M\oreover, the produced amount of CO and H_2 in Ni-Co-doped carrier is comparable to the other state-of-the-art oxygen carrying-catalyst (Table 1). Considering that the doping concentration is low, it was thought that the change in the surface of the co-doped carrier had accelerated the reaction kinetics with CH_4 and CO_2, resulting in improved performance compared to the undoped carrier. In the case of the Ni doped oxygen carrier, its fuel conversion is found to be comparable to that of the co-doped one. However, upon repeated redox cycling, the H_2/CO ratio exceeds 2, indicating the excess formation of H_2 from the coking reaction ($CH_{4(g)} \rightarrow C_{(s)} + 2 H_{2(g)}$), a result that is consistent with our previous findings. On the other hand, Co doped oxygen exhibits lower fuel conversion activity ($\sim 50\%$) compared to both co-doped and Ni doped ones with undesirable H_2/CO ratio (~ 1.6). These findings demonstrate that the co-doping strategy leads to the successful modification of pristine oxygen carriers, once again.

3.4. Evolution of catalyst under the redox condition

Various gases (CH_4, CO_2) were injected into the synthesized oxygen carrier. As indicated by the SEM images after exposure to CH_4, the Ni-Co-doped sample showed numerous emerging nanoparticles on its surface, which were absent in the bare sample (Fig. 6a, Fig. S3, and S4). In the presence of CH_4, Ni and Co in the oxide are readily reduced and rise to the surface of the host oxide, simultaneously forming metal nanoparticles (Fig. S5). Ni and Co may serve as nucleation seeds or the catalyst for hydrogen spillover, thus enabling the formation of the larger amount of nanoparticles, which does not occur in the bare carrier consisting of Fe alone. [38–40] These nanoparticles will facilitate gas-solid reactions by serving as new active sites for CH_4 adsorption and dissociation. [41] Furthermore, the ex-solved particle will ease oxygen ion migration from the bulk lattice. [42,43] The Raman spectrum of the oxygen carriers subsequent to the CH_4 injection step reveals that the Ni-Co doped sample shows broadened peaks in B_{1g} mode ($\nu = 625 \sim 750$ cm^{-1}) and reduced symmetry in $A_{g(3)}$ peak ($\nu = 380 \sim 550$ cm^{-1}) compared to the bare sample (Fig. S6). These peaks are associated with the BO_6 octahedral in perovskite oxide, suggesting that the Ni-Co doped sample contains a significant number of oxygen vacancies and distortions after reduction. [44,45] Eventually, the ex-solved particles are likely to have facilitated overall kinetics in lattice oxygen loss.

Subsequently, to observe the behavioral changes of the oxygen carrier under oxidizing conditions, CO_2 was injected after CH_4. Noticeably, smaller nanoparticles on the Ni-Co-doped sample were present (Fig. 6b, ref Fig. S7 for bare sample); these can influence the CO_2 splitting process. It is expected that the surface nanoparticles became smaller due to changes in the composition under CO_2 atmosphere. Based on verified thermodynamic calculations (Table S2), it was shown that Fe can readily oxidize with CO_2, whereas Ni and Co cannot. Thus, the following circumstances may arise during the redox cycle: mainly, an Fe-Ni-Co alloy (there could be other type of metal nanoparticle such as NiFe, CoFe, Fe) is ex-solved in the CH_4 injection step and is then automatically replaced as a Ni-Co alloy during the CO_2 splitting step, because Fe is selectively dissolved into the host oxide (Fig. 6c). Our hypothesis was clearly confirmed with the HAADF-EDX (Fig. 6d). Also, a quantitative description of the chemical and structural changes of iron in the material was obtained by coupling XANES spectroscopy with Mössbauer spectroscopy and XRD.

X-ray absorption spectroscopy has been performed to acquire precise information on the chemical state of the transition metals. The almost total occupation of Fe in the B-site together with the close proximity of the absorption K-edges of Fe, Co and Ni (7112, 7709, and 8333 eV,
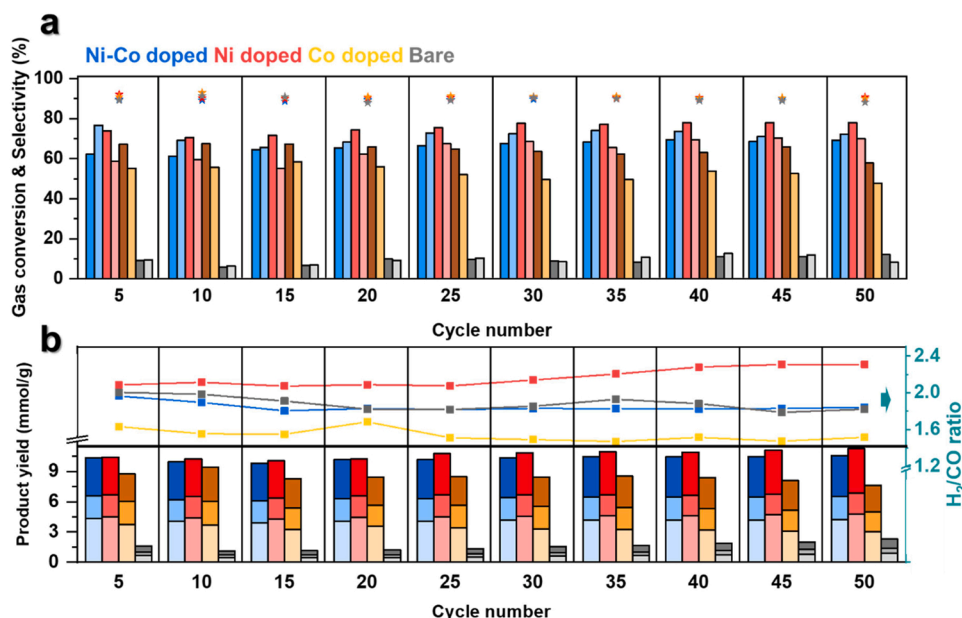
Fig. 5. Multiple redox cycle test results of doped and pristine oxygen carriers. (Blue: Ni-Co doped, Red: Ni doped, Yellow: Co doped, Gray: Bare) (a) Gas conversion and CO selectivity of samples. The deep-colored bar presents the CH_4 conversion and the light-colored bar shows the CO_2 conversion. Star symbols present CO selectivity. (b) The actual amount of the product during the cycle test. Each product is stacked together in a single column (Order from the bottom to top: H_2 from CH_4 reforming, CO from CH_4 reforming, CO from CO_2 splitting). The line graph above the column shows H_2/CO ratio trends following the cycle numbers.

Table 1

Comparison of syngas producibility with other literatures. ([a] Obtained by considering the available amount of lattice oxygen before the carbon coking occurs at the CH_4 atmosphere. [b] Obtained from CO_2-TPO measurement.).

Method	Chemical Looping Process					Solar Thermochemical Reaction		
Selected Work	This work	J. Am. Chem. Soc., 2020, **142**, 11540–11549.	ACS Catal., 2020, **10**, 9420–9430.	Energy Environ. Sci., 2018, **11**, 648–659.	Angew. Chem. Int. Ed., 2020, **59**, 2–12.	Energy Environ. Sci., 2018, **11**, 3256–3265.	Energy Environ. Sci., 2018, **11**, 2172–2178.	Energy Environ. Sci., 2012, **5**, 6098–6103.
Catalyst	$La_{0.6}Ca_{0.4}Fe_{0.95}Ni_{0.025}Co_{0.025}O_3$	$La_{0.5}Ce_{0.5}FeO_3$	$La_{0.5}Sr_{0.5}Fe_{0.8}Al_{0.2}O_3$	$La_{0.6}Ca_{0.4}Fe_{0.4}Mn_{0.6}O_3$	$La_{0.8}Ce_{0.1}Ni_{0.4}Ti_{0.6}O_3$	$BaCe_{0.25}Mn_{0.75}O_3$	$(FeMgCoNi)O_x$	CeO_2
Reactants	5% CH_4, 5% CO_2	10% CH_4, 10% CO_2	5% CH_4, 5% O_2	10% H_2, 10% CO_2	5% CH_4, 5% O_2	40% H_2O	~100% H_2O	85% H_2O + 15% CO_2
Reaction temperature	850 °C	850 °C	900 °C	550 °C	650 °C	1350 °C (Red), 850 °C (Oxi)	1300 °C (Red), 800 °C (Oxi)	1650 °C (Red), 930 °C (Oxi)
Loading mass of oxygen carrier (g)	0.2	0.8	0.1	-	0.3	-	-	-
Effective oxygen storage capacity (umol g^{-1})	2780[a]	-	2700[a]	970[b]	1780	-	-	-
Product yield (umol g^{-1})	6000 (syngas) + 4000 (CO)	4000 (syngas) + 1500 (CO)	-	450 (CO)	2500 (syngas)	130 (H$_2$)	123 (H$_2$)	170 (H$_2$) + 90 (CO)

respectively) did not allow to study the Co and Ni dopants due to signal superimposition. Therefore, XANES spectroscopy has been performed only at the Fe K-edge on the as-synthesized, reduced and re-oxidized perovskite oxides samples (Fig. 7a). From the linear combination fitting (LCF) analysis the Fe speciation in the reduced and re-oxidized material was determined using the spectra of the as-synthesized material, metallic Fe, FeO, and Fe_2O_3 (Fig. 7b and S8). In the reduced sample a significant decrease of the white line as well as an increase of the signal at 7115 eV is noticed resembling the features of the Fe^0 spectrum (Fig. 7b). LCF analysis indicated that almost 40% of the available Fe has been reduced to Fe^0 (Fig. 7c). Interestingly, once the perovskite material has been exposed to the mild oxidative CO_2 atmosphere, the whole metallic Fe content turned back to the ferric state. From the shape of the white line it looks like that the Fe^{3+} is back into a perovskite chemical environment (Fig. 7b). Unfortunately, the aforementioned signal superposition with Co and Ni prevented to retrieve more precise information by EXAFS. In order to tackle this aspect, Mössbauer spectroscopy was performed on the three systems. The spectrum of the pristine material (Fig. S9) consists in the superimposition of a broad and not well resolved sextet and an asymmetric doublet. The sextet has the typical features of a relaxation spectrum, indicating that the sample is near to its magnetic order-disorder transition. As such relaxation component does not allow a reasonable fit of the experimental data, no information about the Fe local interactions can be obtained for this material. After reduction (Fig. 7d), the spectrum is described by the superimposition of different magnetically coupled components, together with paramagnetic/superparamagnetic ones. The best fit was obtained by using five components: three ascribable to magnetically ordered Fe nuclei (sextets) and another two, a doublet and a singlet, due to non-magnetically coupled species. The hyperfine parameters are reported in Table S4. The most intense sextet (55%) can be reasonably attributed to electron-rich Fe nuclei, such as metallic alpha-Fe and/or a Fe-alloy, in good agreement with XANES data. The other two can be ascribed to Fe^{3+} in an octahedral environment. Considering the B values of these two sextets, the one with the highest B could be associated with $LaFeO_3$ while the other can be representative of Fe(III) oxides. Concerning the doublet and the singlet, that account for the 4% of the total area, they can be likely attributed to small fractions of perovskite and metallic Fe/alloy in superparamagnetic regime. Finally, the oxidizing treatment of the reduced material promotes a drastic transformation of the local interaction at the Fe nuclei (Fig. 7e). The Mössbauer spectrum consists in the superimposition of three different magnetically coupled components. The best fitting was achieved by three sextets: two ascribable to octahedral Fe(III) and one to tetrahedral Fe(III). As in the previous sample, the sextet with the highest B can be ascribed to $LaFeO_3$. The other two can be assigned to presence of a spinel phase, likely magnetite or maghemite. It is worth to observe that all the metallic Fe, contained in the reduced sample, is fully oxidized to Fe(III) in good agreement with the XANES analyses. To shed lights into the structural changes during reduction and re-oxidation processes, XRD was measured after each treatment. Upon reduction of the phase pure $La_{0.6}Ca_{0.4}Fe_{0.95}Co_{0.025}Ni_{0.025}O_{3-\delta}$ material, exsolution of Fe-alloys takes place along with the formation of a La_2O_3 and Ca-enriched $La_{1-x}Ca_xFeO_{3-\delta}$ (with x > 0.4) phase originated from the structural rearrangement of the parental material. Interestingly, after the CO_2-driven oxidation the signals of the metallic components disappeared and iron was reincorporated into the perovskite structure $LaFeO_3$ and a spinel phase, in good agreement with Mössbauer data. Eventually, the ex-solved alloy nanoparticles may be responsible for the successful enhancement that occurred during the screening experiments, in a long-term redox test. Not only with that, because Fe could be reincorporated into the host oxide, the reducibility of the parent oxide could also be maintained without critical degradation due to an incomplete phase recovery. [46] To determine whether the ex-solved iron species function as a redox pair, we have loaded 5 mol % of NiCo via wet impregnation method on the pristine oxygen carrier and conducted multiple cycle tests. Fig. S10 shows the fuel conversion
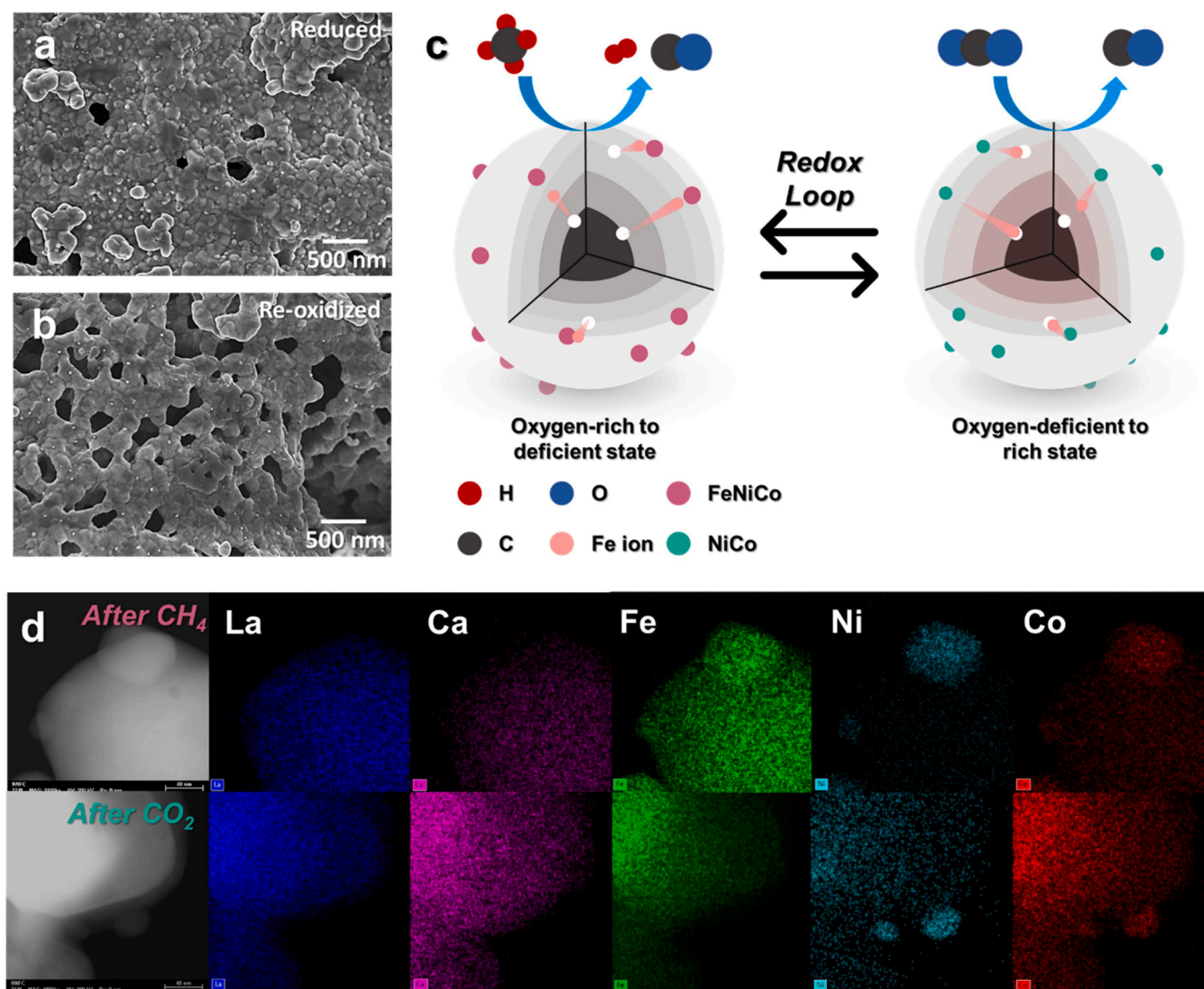
Fig. 6. SEM images of samples, (a) surface of the co-doped carrier after CH$_4$ annealing. (b) CO$_2$ treated surface right after the CH$_4$ oxidation. (c) Proposed concept illustration of catalyst evolution during the operation. (d) HADDF-EDS analysis of Ni-Co doped oxygen carrier after CH$_4$ thermal treatment and after sequential CO$_2$ regeneration.

activity of NiCo impregnated oxygen carrier. It shows around 50% of fuel conversion and 80% of CO selectivity, which is lower than the Ni-Co doped one. Furthermore, as depicted in Fig. S11, while there were no significant changes in crystal structure of the impregnated one, the co-doped carrier exhibited a considerably greater abundance of new phases, including metallic iron and La$_2$O$_3$. Based on the differences in activity and XRD patterns, it is thought that iron serves as a redox pair in (La, Ca)FeO$_{3-\delta}$ based oxygen carrier and ex-solution will far reinforce the redox activity of lattice oxygen.

The synergetic effect of alloys in the dry reforming of methane (DRM) has been discussed in the literature. Ni readily activates C-H bonds in hydrocarbons; however, it undergoes carbon deposition due to the low activity towards CO$_2$. [47] On the other hand, Co shows low CH$_4$ reactivity, and kinetic competition occurs between CH$_4$ and CO$_2$ owing to its high CO$_2$ affinity. [48,49] Thus, the alloy state can show coke resistance through the increased reducibility and hydrocarbon reactivity, thereby being more effectively utilized in DRM conditions by utilizing the benefit of each element Furthermore, it was recently reported that the ex-solved Fe-Ni-Co alloy possesses excellent gas activation in DRM due to the modulation of the d-band center of metals. [50] Similarly, our Ni-Co-doped carrier showed improved coking resistance

and CH$_4$ reactivity compared to when the two elements were doped independently. In addition, it is expected that the alloy will sufficiently capture CO$_2$ owing to the modified oxophilicity of the ex-solved nanoparticles. [51,52] Towards the end of the operation, the particles were still preserved with a negligible size increase (Fig. S12), suggesting high thermal stability imparted by the backbone-anchored characteristic. [53–56].

4. Conclusion

In summary, we used a Sr-free perovskite oxide as an oxygen carrier as well as a catalyst for the CLR coupled with a CO$_2$ splitting reaction. Doping the oxygen carrier with only 5 at% Ni-Co (2.5 at% each) greatly increased the gas conversion by 6 times compared to the bare oxygen carrier. The performance here relies on the high-performance level, and the activities were maintained under harsh conditions (850 °C for 50 redox cycles). We concluded that this improvement was due to the ex-solved nanoparticles under a reducing atmosphere. The Ni-Co-doped sample exhibited improved coke resistance and CH$_4$ reactivity stemming from the synergistic effect of the Fe-Ni-Co alloy. In particular, Fe selectively reunited with the bulk support under a CO$_2$ atmosphere, and
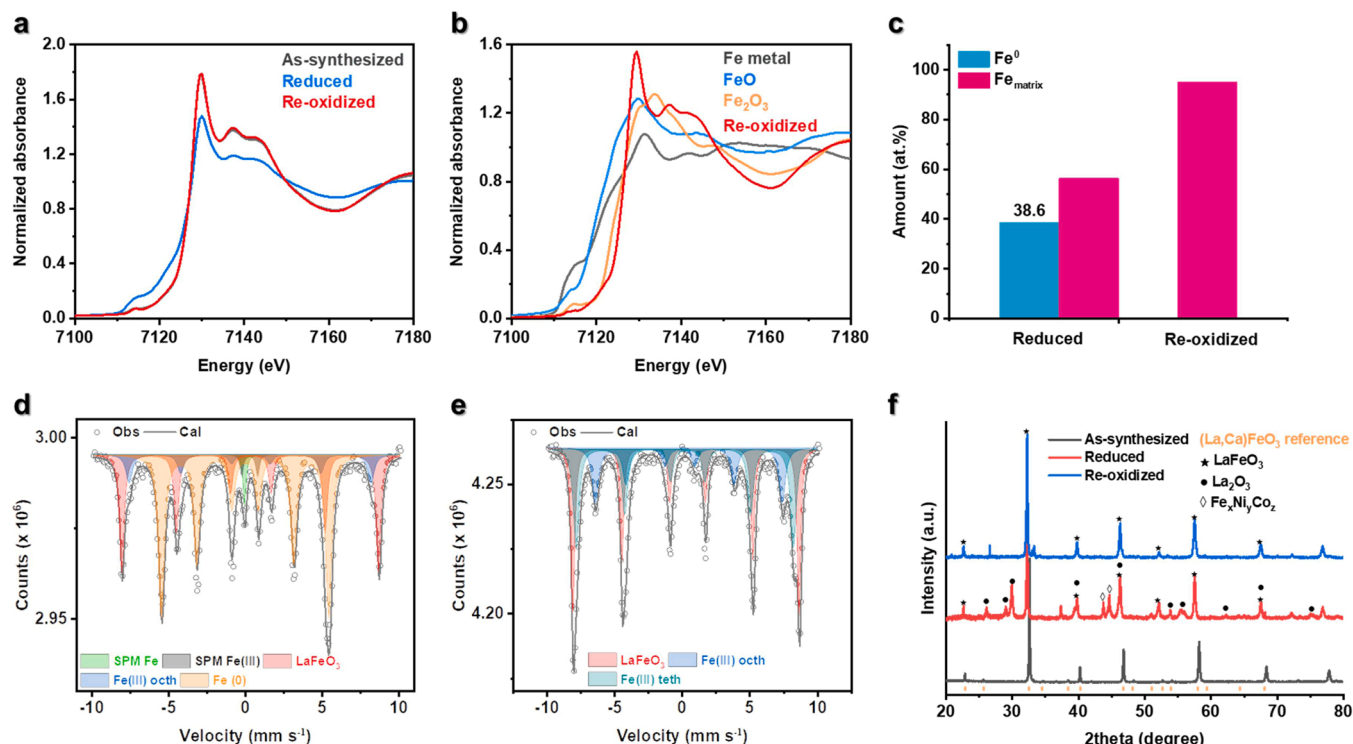
Fig. 7. (a) XANES spectra of the Fe K-edge for the pristine, reduced and re-oxidized materials. (b) Reference spectra of the employed standards and (c) result of the linear combination fitting. ^{57}Fe Mössbauer spectra along with the different components of the (d) reduced and (e) re-oxidized materials. (f) XRD patterns of the pristine, reduced and re-oxidized materials.

the Ni-Co alloy appeared to promote CO_2 splitting by continually remaining on the surface. Involved with the rocking chair-like movement of Fe ions, the ex-solved nanoparticle will be given an ideal state by themselves during repeated CH_4/CO_2 redox cycles. Overall, the ex-solution process showcases the capability of $La_{0.6}Ca_{0.4}FeO_{3-\delta}$ as an excellent redox catalyst as well as an oxygen carrier per se. In addition, our study suggested rational approaches by which to control ex-solved alloys. For ex-solution to be a new avenue of the catalyst designing scenario, further experiments and thermodynamic considerations are required to modulate the desired ratio of the nanoparticle elements. This, in turn, will thrust the application of a material with a single composition to various catalytic reactions, including fuel cells, water splitting, and three-way catalysts through the composition control of ex-solution catalyst.

CRediT authorship contribution statement

DongHwan Oh: Conceptualization, Methodology, Writing – original draft. **Filippo Colombo**: XAS analysis, Writing – review & editing. **Luca Nodari**: Mössbauer analysis, review & editing. **Jun Hyuk Kim**: Raman spectra analysis. **Jun Kyu Kim**: Investigation. **Siwon Lee**: Interpretation of the mass spectra results, Investigation. **Seung Hyun Kim**: Investigation. **Sangwoo Kim**: Investigation. **Dae-Kwang Lim**: Validation. **Jongsu Seo**: Investigation. **Simone Mascotto**: Supervision, Project administration, Funding acquisition, Writing – review & editing. **Woo-Chul Jung**: Supervision, Project administration, Funding acquisition, Writing – review & editing.

Declaration of Competing Interest

The authors declare that they have no known competing financial interests or personal relationships that could have appeared to influence the work reported in this paper.

Data availability

No data was used for the research described in the article.

Appendix A. Supporting information

Supplementary data associated with this article can be found in the online version at doi:10.1016/j.apcatb.2023.122745.

References

[1] Office of Fossil Energy and Carbon Management, DOE announces more than $10 milion for advanced combustion systems research, (2016) ⟨https://www.energy.gov/fecm/articles/doe-announces-more-10-million-advanced-combustion-systems-research⟩.

[2] W.C. Chueh, Z. Shao, S.M. Haile, Tunability of propane conversion over alumina supported Pt and Rh catalysts, Top. Catal. 46 (2007) 402–411, https://doi.org/10.1007/s11244-007-9012-9.

[3] A.L. Sauvet, J.T.S. Irvine, Catalytic activity for steam methane reforming and physical characterisation of La1-xSrxCr1-yNi yO3-δ, Solid State Ion. 167 (2004) 1–8, https://doi.org/10.1016/j.ssi.2003.11.021.

[4] W.C. Chueh, C. Falter, M. Abbott, D. Scipio, P. Furler, S.M. Haile, A. Steinfeld, High-flux solar-driven thermochemical dissociation of CO2 and H2O using nonstoichiometric ceria, Science 330 (2010) 1797–1801, https://doi.org/10.1126/science.1197834.

[5] S. Zoller, E. Koepf, D. Nizamian, M. Stephan, A. Patané, P. Haueter, M. Romero, J. González-Aguilar, D. Lieftink, E. de Wit, S. Brendelberger, A. Sizmann, A. Steinfeld, A solar tower fuel plant for the thermochemical production of kerosene from H2O and CO2, Joule 6 (2022) 1606–1616, https://doi.org/10.1016/j.joule.2022.06.012.

[6] J. Seo, N. Tsvetkov, S.J. Jeong, Y. Yoo, S. Ji, J.H. Kim, J.K. Kang, W.C. Jung, Gas-permeable inorganic shell improves the coking stability and electrochemical reactivity of Pt toward methane oxidation, ACS Appl. Mater. Interfaces 12 (2020) 4405–4413, https://doi.org/10.1021/acsami.9b16410.

[7] S. Sengodan, S. Choi, A. Jun, T.H. Shin, Y.W. Ju, H.Y. Jeong, J. Shin, J.T.S. Irvine, G. Kim, Layered oxygen-deficient double perovskite as an efficient and stable anode for direct hydrocarbon solid oxide fuel cells, Nat. Mater. 14 (2015) 205–209, https://doi.org/10.1038/nmat4166.

[8] X. Zhang, Y. Jiang, X. Hu, L. Sun, Y. Ling, High performance proton-conducting solid oxide fuel cells with a layered perovskite GdBaCuCoO5+x cathode, Electron. Mater. Lett. 14 (2018) 147–153, https://doi.org/10.1007/s13391-018-0023-4.

[9] X. Zhu, Q. Imtiaz, F. Donat, C.R. Müller, F. Li, Chemical looping beyond combustion – a perspective, Energy Environ. Sci. 13 (2020) 772–804, https://doi.org/10.1039/C9EE03793D.

[10] X. Zhang, Y. Xu, Y. Liu, L. Niu, Y. Diao, Z. Gao, B. Chen, J. Xie, M. Bi, M. Wang, D. Xiao, D. Ma, C. Shi, A novel Ni–MoCxOy interfacial catalyst for syngas production via the chemical looping dry reforming of methane, Chem (2022) 1–15, https://doi.org/10.1016/j.chempr.2022.09.007.

[11] L. Qin, Z. Cheng, M. Guo, M. Xu, J.A. Fan, L.S. Fan, Impact of 1% lanthanum dopant on carbonaceous fuel redox reactions with an iron-based oxygen carrier in chemical looping processes, ACS Energy Lett. 2 (2017) 70–74, https://doi.org/10.1021/acsenergylett.6b00511.

[12] A. Löfberg, J. Guerrero-Caballero, T. Kane, A. Rubbens, L. Jalowiecki-Duhamel, Ni/CeO2 based catalysts as oxygen vectors for the chemical looping dry reforming of methane for syngas production, Appl. Catal. B Environ. 212 (2017) 159–174, https://doi.org/10.1016/j.apcatb.2017.04.048.

[13] X. Zhu, K. Li, L. Neal, F. Li, Perovskites as geo-inspired oxygen storage materials for chemical looping and three-way catalysis: a perspective, ACS Catal. 8 (2018) 8213–8236, https://doi.org/10.1021/acscatal.8b01973.

[14] D. Sastre, D.P. Serrano, P. Pizarro, J.M. Coronado, Chemical insights on the activity of La1-xSrxFeO3 perovskites for chemical looping reforming of methane coupled with CO2-splitting, J. CO2 Util. 31 (2019) 16–26, https://doi.org/10.1016/j.jcou.2019.02.013.

[15] D.D. Taylor, N.J. Schreiber, B.D. Levitas, W. Xu, P.S. Whitfield, E.E. Rodriguez, Oxygen storage properties of La1− x Sr x FeO 3−δ for chemical-looping reactions—an in situ neutron and synchrotron X-ray study, Chem. Mater. 28 (2016) 3951–3960, https://doi.org/10.1021/acs.chemmater.6b01274.

[16] L.M. Neal, A. Shafiefarhood, F. Li, Dynamic methane partial oxidation using a Fe 2 O 3 @La 0.8 Sr 0.2 FeO 3-δ core–shell redox catalyst in the absence of gaseous oxygen, ACS Catal. 4 (2014) 3560–3569, https://doi.org/10.1021/cs5008415.

[17] F. He, X. Li, K. Zhao, Z. Huang, G. Wei, H. Li, The use of La1-xSrxFeO3 perovskite-type oxides as oxygen carriers in chemical-looping reforming of methane, Fuel 108 (2013) 465–473, https://doi.org/10.1016/j.fuel.2012.11.035.

[18] Y. Kim, S.J. Jeong, B. Koo, S. Lee, N.W. Kwak, W. Jung, Study of the surface reaction kinetics of (La,Sr)MnO 3−δ oxygen carriers for solar thermochemical fuel production, J. Mater. Chem. A 6 (2018) 13082–13089, https://doi.org/10.1039/C8TA01939H.

[19] B. Koo, H. Kwon, Y. Kim, H.G. Seo, J.W. Han, W. Jung, Enhanced oxygen exchange of perovskite oxide surfaces through strain-driven chemical stabilization, Energy Environ. Sci. 11 (2018) 71–77, https://doi.org/10.1039/c7ee00770a.

[20] M.E. Gálvez, R. Jacot, J. Scheffe, T. Cooper, G. Patzke, A. Steinfeld, Physico-chemical changes in Ca, Sr and Al-doped La-Mn-O perovskites upon thermochemical splitting of CO2 via redox cycling, Phys. Chem. Chem. Phys. 17 (2015) 6629–6634, https://doi.org/10.1039/c4cp05898d.

[21] N. Tsvetkov, Q. Lu, L. Sun, E.J. Crumlin, B. Yildiz, Improved chemical and electrochemical stability of perovskite oxides with less reducible cations at the surface, Nat. Mater. 15 (2016) 1010–1016, https://doi.org/10.1038/nmat4659.

[22] H.S. Lim, M. Lee, D. Kang, J.W. Lee, Role of transition metal in perovskites for enhancing selectivity of methane to syngas, Int. J. Hydrog. Energy 43 (2018) 20580–20590, https://doi.org/10.1016/j.ijhydene.2018.09.067.

[23] W. Lee, J.W. Han, Y. Chen, Z. Cai, B. Yildiz, Cation size mismatch and charge interactions drive dopant segregation at the surfaces of manganite perovskites, J. Am. Chem. Soc. 135 (2013) 7909–7925, https://doi.org/10.1021/ja3125349.

[24] G. Tsekouras, H. Ménard, J.T.S. Irvine, D. Neagu, D.N. Miller, In situ growth of nanoparticles through control of non-stoichiometry, Nat. Chem. 5 (2013) 916–923, https://doi.org/10.1038/nchem.1773.

[25] J.H. Kim, J.K. Kim, H.G. Seo, D.K. Lim, S.J. Jeong, J. Seo, J. Kim, W.C. Jung, Ex-Solved Ag nanocatalysts on a sr-free parent scaffold authorize a highly efficient route of oxygen reduction, Adv. Funct. Mater. 30 (2020) 1–9, https://doi.org/10.1002/adfm.202001326.

[26] J.K. Kim, Y. Jo, S. Kim, B. Koo, J.H. Kim, B. Kim, W. Jung, Exceptional tunability over size and density of spontaneously formed nanoparticles via nucleation dynamics, ACS Appl. Mater. Interfaces 12 (2020) 24039–24047, https://doi.org/10.1021/acsami.0c05215.

[27] S. Otto, K. Kousi, D. Neagu, L. Bekris, J. Janek, I.S. Metcalfe, Exsolved nickel nanoparticles acting as oxygen storage reservoirs and active sites for redox CH 4 conversion, acsaem.9b01267, ACS Appl. Energy Mater. (2019), https://doi.org/10.1021/acsaem.9b01267.

[28] K. Kousi, D. Neagu, L. Bekris, E.I. Papaioannou, I.S. Metcalfe, Endogenous nanoparticles strain perovskite host lattice providing oxygen capacity and driving

[29] Q. Jiang, Y. Gao, V.P. Haribal, H. Qi, X. Liu, H. Hong, H. Jin, F. Li, Mixed conductive composites for 'Low-Temperature' thermo-chemical CO2 splitting and syngas generation, J. Mater. Chem. A (2020) 13173–13182, https://doi.org/10.1039/d0ta03232h.

[30] O. Mihai, D. Chen, A. Holmen, Chemical looping methane partial oxidation: the effect of the crystal size and O content of LaFeO3, J. Catal. 293 (2012) 175–185, https://doi.org/10.1016/j.jcat.2012.06.022.

[31] Z. Bian, S. Das, M.H. Wai, P. Hongmanorom, S. Kawi, A review on bimetallic nickel-based catalysts for CO2 reforming of methane, ChemPhysChem 18 (2017) 3117–3134, https://doi.org/10.1002/cphc.201700529.

[32] J.R. Scheffe, M. Welte, A. Steinfeld, Thermal reduction of ceria within an aerosol reactor for H2O and CO2 splitting, Ind. Eng. Chem. Res. 53 (2014) 2175–2182, https://doi.org/10.1021/ie402620k.

[33] L. Zhang, W. Xu, J. Wu, Y. Hu, C. Huang, Y. Zhu, M. Tian, Y. Kang, X. Pan, Y. Su, J. Wang, X. Wang, Identifying the role of a-site cations in modulating oxygen capacity of iron-based perovskite for enhanced chemical looping methane-to-syngas conversion, ACS Catal. 10 (2020) 9420–9430, https://doi.org/10.1021/acscatal.0c01811.

[34] B. Kayaalp, S. Lee, K. Klauke, J. Seo, L. Nodari, A. Kornowski, W.C. Jung, S. Mascotto, Template-free mesoporous La0.3Sr0.7FexTi1-xO3±∆ with superior oxidation catalysis performance, Appl. Catal. B Environ. 245 (2019) 536–545, https://doi.org/10.1016/j.apcatb.2018.12.077.

[35] P. Cho, T. Mattisson, A. Lyngfelt, Comparison of iron-, nickel-, copper- and manganese-based oxygen carriers for chemical-looping combustion, Fuel 83 (2004) 1215–1225, https://doi.org/10.1016/j.fuel.2003.11.013.

[36] D. Marxer, P. Furler, M. Takacs, A. Steinfeld, Solar thermochemical splitting of CO2 into separate streams of CO and O2 with high selectivity, stability, conversion, and efficiency, Energy Environ. Sci. 10 (2017) 1142–1149, https://doi.org/10.1039/c6ee03776c.

[37] S. Dey, C.N.R. Rao, Splitting of CO2 by manganite perovskites to generate CO by solar isothermal redox cycling, ACS Energy Lett. 1 (2016) 237–243, https://doi.org/10.1021/acsenergylett.6b00122.

[38] S. Joo, O. Kwon, K. Kim, S. Kim, H. Kim, J. Shin, H.Y. Jeong, S. Sengodan, J.W. Han, G. Kim, Cation-swapped homogeneous nanoparticles in perovskite oxides for high power density, Nat. Commun. 10 (2019) 1–9, https://doi.org/10.1038/s41467-019-08624-0.

[39] S.L. Zhang, H. Wang, M.Y. Lu, A.P. Zhang, L.V. Mogni, Q. Liu, C.X. Li, C.J. Li, S. A. Barnett, Cobalt-substituted SrTi0.3Fe0.7O3-δ a stable high-performance oxygen electrode material for intermediate-temperature solid oxide electrochemical cells, Energy Environ. Sci. 11 (2018) 1870–1879, https://doi.org/10.1039/c8ee00449h.

[40] T. Zhu, H.E. Troiani, L.V. Mogni, M. Han, S.A. Barnett, Ni-Substituted Sr(Ti,Fe)O3 SOFC anodes: achieving high performance via metal alloy nanoparticle exsolution, Joule 2 (2018) 478–496, https://doi.org/10.1016/j.joule.2018.02.006.

[41] S. Lee, H. Ha, K.T. Bae, S. Kim, H. Choi, J. Lee, J.H. Kim, J. Seo, J.S. Choi, Y.R. Jo, B.J. Kim, Y. Yang, K.T. Lee, H.Y. Kim, W.C. Jung, A measure of active interfaces in supported catalysts for high-temperature reactions, Chem 8 (2022) 815–835, https://doi.org/10.1016/j.chempr.2021.11.024.

[42] G.N. Vayssilov, Y. Lykhach, A. Migani, T. Staudt, G.P. Petrova, N. Tsud, T. Skála, A. Bruix, F. Illas, K.C. Prince, V. Matolín, K.M. Neyman, J. Libuda, Support nanostructure boosts oxygen transfer to catalytically active platinum nanoparticles, Nat. Mater. 10 (2011) 310–315, https://doi.org/10.1038/nmat2976.

[43] A. Shafiefarhood, J. Zhang, L.M. Neal, F. Li, Rh-promoted mixed oxides for "low-temperature" methane partial oxidation in the absence of gaseous oxidants, J. Mater. Chem. A 5 (2017) 11930–11939, https://doi.org/10.1039/c7ta01398a.

[44] M. Gu, J.M. Rondinelli, Role of orbital filling on nonlinear ionic Raman scattering in perovskite titanates, Phys. Rev. B 95 (2017), 024109 doi:10.1103.PhysRevB.95.024109.

[45] M.V. Abrashev, J. Bäckström, L. Börjesson, V.N. Popov, R.A. Chakalov, N. Kolev, R.-L. Meng, M.N. Iliev, Raman spectroscopy of CaMnO3: mode assignment and relationship between Raman line intensities and structural distortions, Phys. Rev. B 65 (2002), 184301 doi.org/10.1103.PhysRevB.65.184301.

[46] D. Hosseini, F. Donat, P.M. Abdala, S.M. Kim, A.M. Kierzkowska, C.R. Müller, Reversible exsolution of dopant improves the performance of Ca2Fe2O 5 for chemical looping hydrogen production, ACS Appl. Mater. Interfaces 11 (2019) 18276–18284, https://doi.org/10.1021/acsami.8b16732.

[47] M.A. Serrer, A. Gaur, J. Jelic, S. Weber, C. Fritsch, A.H. Clark, E. Saraçi, F. Studt, J. D. Grunwaldt, Structural dynamics in Ni-Fe catalysts during CO2 methanation-role of iron oxide clusters, Catal. Sci. Technol. 10 (2020) 7542–7554, https://doi.org/10.1039/d0cy01396j.

[48] A.I. Tsiotsias, B. Ehrhardt, B. Rudolph, L. Nodari, S. Kim, W.C. Jung, N. D. Charisiou, M.A. Goula, S. Mascotto, Bimetallic exsolved heterostructures of controlled composition with tunable catalytic properties, ACS Nano 16 (2022) 8904–8916, https://doi.org/10.1021/acsnano.1c11111.

[49] Z. Wu, B. Yang, S. Miao, W. Liu, J. Xie, S. Lee, M.J. Pellin, D. Xiao, D. Su, D. Ma, Lattice strained Ni-Co alloy as a high-performance catalyst for catalytic dry reforming of methane, ACS Catal. 9 (2019) 2693–2700, https://doi.org/10.1021/acscatal.8b02821.

[50] S. Joo, K. Kim, O. Kwon, J. Oh, H.J. Kim, L. Zhang, J. Zhou, J.-Q. Wang, H. Y. Jeong, J.W. Han, G. Kim, Enhancing thermocatalytic activities by upshifting the d-band center of exsolved Co-Ni-Fe ternary alloy nanoparticles for the dry reforming of methane, Angew. Chem. 133 (2021) 16048–16055, https://doi.org/10.1002/ange.202101335.

[51] B. AlSabban, L. Falivene, S.M. Kozlov, A. Aguilar-Tapia, S. Ould-Chikh, J. L. Hazemann, L. Cavallo, J.M. Basset, K. Takanabe, In-operando elucidation of bimetallic CoNi nanoparticles during high-temperature CH_4/CO_2 reaction, Appl. Catal. B Environ. 213 (2017) 177–189, https://doi.org/10.1016/j.apcatb.2017.04.076.

[52] L. Li, D.H. Anjum, H. Zhu, Y. Saih, P.V. Laveille, L. D'Souza, J.M. Basset, Synergetic effects leading to coke-resistant NiCo bimetallic catalysts for dry reforming of methane, ChemCatChem 7 (2015) 427–433, https://doi.org/10.1002/cctc.201402921.

[53] J.H. Myung, D. Neagu, D.N. Miller, J.T.S. Irvine, Switching on electrocatalytic activity in solid oxide cells, Nature 537 (2016) 528–531, https://doi.org/10.1038/nature19090.

[54] Y. Gao, D. Chen, M. Saccoccio, Z. Lu, F. Ciucci, From material design to mechanism study: nanoscale Ni exsolution on a highly active A-site deficient anode material for solid oxide fuel cells, Nano Energy 27 (2016) 499–508, https://doi.org/10.1016/j.nanoen.2016.07.013.

[55] D. Neagu, T.-S. Oh, D.N. Miller, H. Ménard, S.M. Bukhari, S.R. Gamble, R.J. Gorte, J.M. Vohs, J.T.S. Irvine, Nano-socketed nickel particles with enhanced coking resistance grown in situ by redox exsolution, Nat. Commun. 6 (2015) 8120, https://doi.org/10.1038/ncomms9120.

[56] S. Jo, B. Sharma, D.-H. Park, J. Myung, Materials and nano-structural processes for use in solid oxide fuel cells: a review, J. Korean Ceram. Soc. 57 (2020) 135–151, https://doi.org/10.1007/s43207-020-00022-3.